

Metal Nanoparticle – Embedded Thin Films for Photonic Sensing

Hala J El-Khozondar, Electrical Engineering and Smart Systems Department, Islamic University of Gaza, Palestine

Waleed S Mohammed, Center of Research in Optoelectronics, Communication and Control Systems (BU-CROCCS), Bangkok University, Pathum Thani, Thailand

© 2022 Elsevier Inc. All rights reserved.

Abstract

The article presents the theoretical investigations on the utilization of thin films formed by a composition of multiple-type metal nanoparticles (NPs) toward the passive optical sensing applications. This is achieved through the manipulation of plasmonic absorption in the nanoparticle-composites by changing the type, size and volume-fraction of the nanoparticles. Achieving passive device is considered by maximizing the “amplitude dynamic range” over a certain part of the visible spectrum. Hence, the Sun light can be used as a source and the subsequent color change is the indication. Two limits are considered: when the size of the particles is much smaller than the wavelength (Maxwells Garnett limit) and when they are comparable to the wavelength. In the first case, the “effective index medium” of the particles embedded in a polymer film is considered where the film thickness and volume fractions of the particles are the main factors while designing the optical sensor. When the size of the particles increases, their effect on the incident light is considered using Mei scattering. In the case of the large particles, the thin film can be formed by a monolayer of one particle or multiple particles. In either limits and configuration, the realized thin film is optimized by maximizing both wavelength and intensity dynamic ranges.

Key Points

- A thin polymer film embedded with small metal nanoparticles and a monolayer of large nanoparticles have been considered the materials for photonic sensing.
- Theoretical analysis in the two cases is done using effective medium theory and Mei scattering.
- Vapor optical sensing is due to the localized surface Plasmon resonance in metal nanoparticles.
- Maximization of optical sensing is achieved in the amplitude dynamic ranges of the sensors.
- Passive optical sensor is understood based on colorimetry.

Introduction

The ability to deposit thin films of various materials is important for the fabrication of modern microelectronic devices and for enabling a variety of investigations of fundamental physical principles. There are many techniques for controllably depositing thin films onto a substrate with thicknesses as small as a few nm (Kumar and J, 2013). Thin films are generally used to improve the surface properties of solids. Transmission, reflection, absorption, hardness, abrasion resistance, corrosion, permeation and electrical behavior are only some of the properties of a bulk material surface that can be improved by using a thin film. Nanotechnology is based on thin film technology. Thin film technologies are mainly divided into physical vapor deposition (PVD) and chemical vapor deposition (CVD) processes (Rao and Shekhawat, 2013).

Nanomaterial, by definition, requires the presence of at least one dimension in the nanometer scale, which can either form naturally or can be synthesized. The term “nanoparticle”, originally named “small particles” was generally known as particulate matter consisting of at least one-dimension of 1–100 nanometers in size (Ngo *et al.*, 2019). Due to this small size, nanoparticles have high surface-to-volume ratios. The high surface-to-volume ratios and quantum-confinement effects give nanoparticles unusual chemical, electrical, electronic, optical, magnetic and mechanical properties that are radically different from those of the bulk materials (Kumar and J, 2013).

This nanosized effect produces an effectively new material with unique optical properties that can be manipulated to the needs of particular applications by altering the structure parameters. With proper design, specific responses can be enhanced to target the desired function such as drug development, water decontamination, information and communication technologies, and the production of stronger and lighter materials (Benelmekki, 2015). In several applications, the nanostructure is used to detect a variation in the environment that causes a change of its optical, chemical, electrical or mechanical properties. For light-matter interaction, this variation could be accounted for a change in the refractive index of the surrounding medium or a direct modification of the structure properties (e.g., refractive index, dimensions, conductivity). This effect alters the response to the incident light, which can be detected as a change in the light intensity or a shift in its wavelength. A practical optical sensor is then formed when the change in the nanostructure response is calibrated to the corresponding amount of change in the environment (Chen *et al.*, 2004).

One of the commonly deserved environmental parameters is the amount of a specific vapor in air, such as the percentage of humidity and the concentration of toxic vapors. Sensing of these vapors is important in many fields such as electronic and chemical industries, optoelectronic device manufacturing, agriculture, medical diagnostics, metrology, and aerospace (Gurban *et al.*, 2015; Buvailo *et al.*, 2011). Developing optical sensors using nanostructures strongly depends to the type of the materials

used in forming these structures. Typically, one can consider either organic or inorganic materials. However, the main focus is on the use of inorganic substances as the building units. These units can take several forms including nanoparticles (Sahi *et al.*, 2018), nanowires (Kuang *et al.*, 2007), nanotubes (Cheng *et al.*, 2011), and nanofibers (Mogera *et al.*, 2014). When considering nanostructures in optical sensing, there are several parameters that can affect the device performance such as bulk material properties, structure geometry and the dimensions. The performance is typically represented by the sensitivity that is defined as the amount of the shift of the detected optical signal divided by the amount of the environmental change. Several types of nanoparticles (NPs) are commonly used in fabricating vapor sensors such as gold (Au) and silver (Ag) NPs in different nanocomposites (Lee *et al.*, 2014; Power *et al.*, 2010; Thiawong *et al.*, 2013; Drabik *et al.*, 2013). Other structures like CuO NPs (Yakubu *et al.*, 2018), ZnO nanorods (Yusof *et al.*, 2018), and nickel (Ni) NPs (Miao *et al.*, 2010) are also used to humidity sensors.

Nanostructures composed of metal and metal oxides, when interacting with light, can experience Surface Plasmon Resonance (SPR) or Localized Surface Plasmon Resonance (LSPR) effects (Liu *et al.*, 2019). SPR occurs when the electron oscillation at the interface matches the propagation constant of the incident light. LSPR occurs when the surface plasmons are localized in the nanoparticles. At the resonance condition, the incident photon energy is absorbed and a reduction of the light intensity is noticed around a specific wavelength. Any change in the refractive index of the surrounding medium causes a shift in the resonance wavelength (McFarland and Van Duyne, 2003).

This article discusses the utilization of thin films formed by nanoparticles toward humidity and vapor sensing applications. When a light passes through a thin film, it experiences multiple reflections from the reflective parallel surfaces of the film. The interference between these reflected or transmitted beams, known as the so-called Fabry-Perot interference, causes the appearance of the peaks and valleys in the spectrum, the locations of which are sensitive to the changes of the surrounding environment.

Nanoparticle-Based Thin Films for Sensing

To use the unique properties of the nanoparticles in optical sensing, the nanoparticles need to be present in a way that light strongly interacts with them and the environment effect can be examined through detectable optical signal. One practical approach is to embed the particles in a medium forming a homogeneous thin film. A thin film causes a clear Fabry-Perot effect where light experiences infinite number of reflections between the upper and lower interfaces. These multiple reflections allow a large number of interactions between light and NPs, as shown in Fig. 1. The total reflection and transmittance are a result of the superposition of the light beams leaking outside. The changes in the environment affect the Fresnel reflection at the top interface causing a detectable shift in the Fabry-Perot response.

Thin Film Formed by Embedding Nanoparticles in a Host Medium

In order to consider a homogeneous thin film formed by foreign particles embedded within a dielectric host medium of thickness d , as depicted in Fig. 1, the particles need to be very small compared to the optical wavelength. The effective medium theory can be applied in this case, as a new medium is formed. The effective medium properties depend on the original host as well as the particles bulk material and concentration (Nielsen, 2003). Accordingly, the effective refractive index of the formed film is given by Eq. (1).

$$n_{eff}^2 = \frac{1 - 2f\eta}{1 + 2f\eta} \quad (1)$$

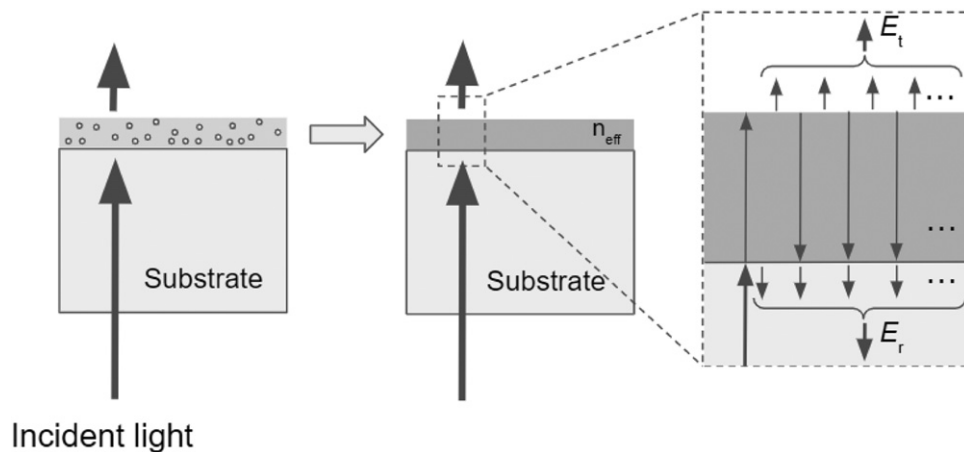


Fig. 1 (a) A thin film formed by impeding nanoparticles in a host medium with thickness d (b) Effective medium approximation of the host with impurities as a homogeneous film with effective index. (c) Fabry-Perot interference caused by infinite reflections inside the film.

In Eq. (1), $\eta = (\epsilon_m - \epsilon_h)/(\epsilon_m + 2\epsilon_h)$, where ϵ_m and ϵ_h are permittivity of the nanoparticles and host permittivity, respectively. When light is normally incident, the multiple reflections with the NPs inside the film form a Fabry-Perot (Fig. 1(c)), where the reflection coefficients at the film/substrate (r_{21}) and film/superstrate (r_{23}) are complex.

The resultant reflection coefficient, $r = |E_r|/|E_i|$, is

$$r = r_{12} + \frac{t_{12}t_{21}r_{23}\exp(i2k_0n_{eff}d)}{1 - r_{23}r_{21}\exp(i2k_0n_{eff}d)} \quad (2)$$

Here, $r_{21} = -r_{12} = (\mu_2n_{eff} - \mu_1n_1)/(\mu_2n_{eff} + \mu_1n_1)$, where n_1 is the refractive index of the substrate; d is the film thickness; and μ_1 and μ_2 denote the permeability of the substrate and the effective medium, respectively. The values of the coefficients μ_1 and μ_2 equal one when the incident light is TE-polarized. For TM-polarized light, these constants are $\mu_1 = 1/n_1^2$ and $\mu_2 = 1/n_{eff}^2$, respectively. The constant k_0 is the free space propagation constant, $k_0 = 2\pi/\lambda$, where λ is the wavelength of the incident light. The reflection coefficient between the film and the surrounding environment is

$$r_{23} = (\mu_2n_{eff} - \mu_3n_3)/(\mu_2n_{eff} + \mu_3n_3) \quad (3)$$

Similarly, the constant μ_3 equals 1 for TE polarized and $1/n_3^2$ for TM polarization where n_3 is the surrounding refractive index. The transmittance coefficient is $t_{mj} = 1 + r_{mj}$, where m and j can be 1, 2 or 3.

Working as an optical sensor, the changes in the environment is represented by the changes in the complex refractive index of the superstrate, n_3 . This alters the Fresnel reflection in Eq. (3). The change of r_{23} with n_3 can be written as

$$\frac{dr_{23}}{dn_3} = \frac{-2\mu_3\mu_2n_{eff}}{(\mu_2n_{eff} + \mu_3n_3)^2} \quad (4)$$

The change in r_{23} affects the total reflection coefficient in Eq. (2). If the phase term is defined as $\phi = 2k_0n_{eff}d$, the rate of change of the reflection in terms of change in the environment can be expressed as

$$\frac{dr}{dn_3} = \frac{dr}{dr_{23}} \frac{dr_{23}}{dn_3} = \left(\frac{t_{12}t_{21}e^{i\phi}}{(1 - r_{23}r_{21}e^{i\phi})^2} \right) \cdot \left(\frac{-2\mu_3\mu_2n_{eff}}{(\mu_2n_{eff} + \mu_3n_3)^2} \right) \quad (5)$$

Simplifying the Eq. (5) for TE - polarization and expanding t_{12} and t_{21} in terms of r and r_{12} ,

$$\frac{dr}{dn_3} = \frac{dr}{dr_{23}} \frac{dr_{23}}{dn_3} = \left(e^{-i\phi} \frac{(r - r_{12})^2}{r_{23}^2(1 - r_{12}^2)} \right) \cdot \left(\frac{-2n_{eff}}{(n_{eff} + n_3)^2} \right) \quad (6)$$

The reflection coefficient r is complex in nature. What is actually measured is the reflectance which is related to r by $R = r \cdot r^*$. The change in the reflectance with n_3 is

$$\frac{dR}{dn_3} = \frac{dr}{dn_3} \cdot r^* + r \cdot \frac{dr^*}{dn_3} \quad (7)$$

If r can be expressed as a general complex number, $r = |r|e^{i\phi}$, the complex conjugate $r^* = |r|e^{-i\phi}$. The derivative of r^* is $\frac{dr^*}{dn_3} = \frac{d|r|}{dn_3}e^{-i\phi} - i|r|\frac{d\phi}{dn_3}e^{-i\phi}$. If the term $\frac{d\phi}{dn_3}$ is real, $\frac{dr^*}{dn_3} = \left(\frac{d|r|}{dn_3}e^{i\phi} + i|r|\frac{d\phi}{dn_3}e^{i\phi} \right)^* = \left(\frac{dr}{dn_3} \right)^*$. Using this assumption and expanding t_{12} and t_{21} in terms of r_{12} , Eq. (7) can be simplified as

$$\frac{dR}{dn_3} = 2\text{Re} \left\{ \frac{dr}{dn_3} \cdot r^* \right\} = -2\text{Re} \left\{ r^* e^{-i\phi} \frac{(r - r_{12})^2}{r_{23}^2(1 - r_{12}^2)} \cdot \left(\frac{2n_{eff}}{(n_{eff} + n_3)^2} \right) \right\} \quad (8)$$

Eq. (8) demonstrates the strong dependency of the sensitivity of the structure on the properties of NPs, represented by the effective refractive index of the film. The term n_{eff} has functional dependence on r , ϕ , r_{12} and r_{23} . Hence, a proper selection of the type of NPs and their volume fraction in the medium can improve the sensing responses.

Structure Response to Environmental Changes

To examine the response of the structure in Fig. 1(a) to the changes in the environment, one can consider a glass substrate with fixed refractive index n_1 . The superstrate index, n_3 , however changes with the presence of vapor; n_3 becomes an effective index composed of air with a certain concentration of water. Its value ranges from 1 to a maximum of 1.33. The change of n_3 due to humidity alters the complex Fresnel reflection coefficient r_{23} , as discussed above. This causes a shift in the total reflection coefficient, r . This affects the reflection spectrum in terms of the peak wavelength location and the maximum amplitude, as illustrated in Fig. 2(a). The plots are calculated for gold NPs in a polymer ($n_h = 1.446$) and a glass substrate ($n_1 = 1.5$) for $f = 0.06$, when TE wave is considered. The reflectance plotted as a function of wavelength for the structure, as in Fig. 1, while using gold nanoparticles in a polymer host ($n_1 = 1.446$), glass substrate ($n_3 = 1.5$) with varying superstrate index from $n_3 = 1$ to 1.3, is shown in Fig. 2.

Fig. 2(b) shows the extracted reflectance at the LSPR peak for all the superstrate indices, e.g., for the case of air, $\lambda = 580.6$ nm. The sensitivity of the structure, $\frac{dR}{dn_3}$, is obtained from the slope of the graph. For the plot in Fig. 2(b), the estimated slope is $\frac{dR}{dn_3} = -0.181$. Using the expression obtained in Eq. (8) and considering n_3 as the middle value of the scan range ($n_3 = 1.15$), the predicted sensitivity is $\frac{dR}{dn_3} = -0.178$, a value close to the calculated value. Looking back at the reflection spectra in Fig. 2(a), the LSPR peak experiences a shift in both amplitude and location when n_3 changes. This effect is ideal for designing an optical sensor

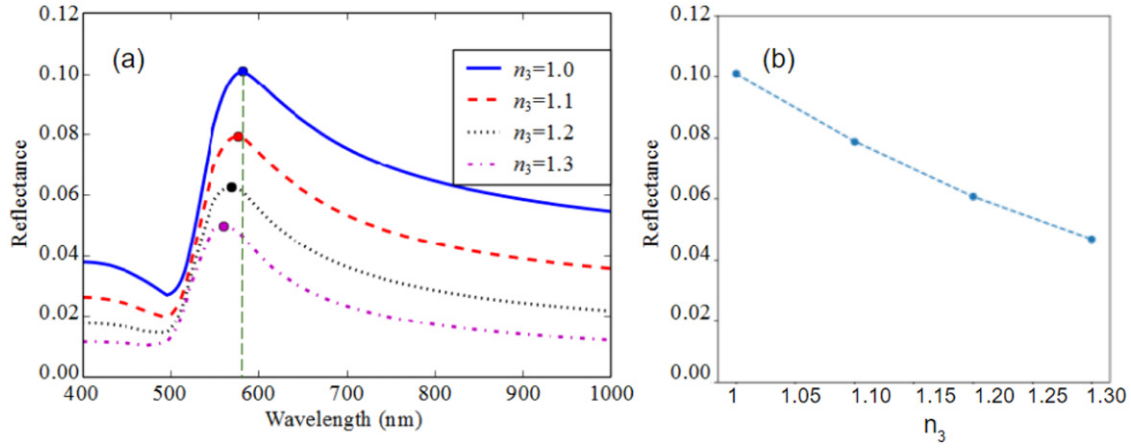


Fig. 2 (a) Calculated reflectance spectrum for the structure in Fig. 1 when using gold nanoparticles in a polymer host ($n_1 = 1.446$), glass substrate ($n_3 = 1.5$) and varying the superstrate index from $n_3 = 1$ to 1.3. The film thickness is set to 80 nm. (b) The Reflectance at the LSPR peak (580.6 nm) as a function of n_3 .

from the point of view signal processing. It is always easy to track such a distinct feature over the operation range. When focusing the analysis on vapor and humidity sensing, the operation range is limited to changes of n_3 from air ($n_3 = 1$) to solution ($n_3 = 1.33$). The maximum change of the system response over this range is defined as “dynamic range”. Based on the LSPR spectra in Fig. 2(a), the intensity dynamic range (*Int. dynamic range*) is the difference of the peak reflectance in percentage when $n_3 = 1.33$ compared to the case of air surrounding.

$$\text{Int. dynamic range} = 100 \cdot (R_{\text{Peak}, n_3 = 1.33} - R_{\text{Peak}, n_3 = 1}) \quad (9)$$

If the response of the NPs film is assumed to be linear, the *Int. dynamic range* $\approx 100 \cdot \Delta n_3 \cdot dR/dn_3$. Using the approximation in Eq. (8), a closed form representation of the dynamic range can be expressed as

$$\text{Int. dynamic range} \approx -200 \cdot \Delta n_3 \text{Re} \left\{ r^* e^{-i\phi} \frac{(r - r_{12})^2}{(1 - r_{12}^2)} \cdot \left(\frac{2n_{\text{eff}}}{(n_{\text{eff}} + n_3)^2} \right) \right\} \quad (10)$$

In Eq. (10), the terms in the group brackets are calculated at a value in the middle of the operation range ($n_3 = 1.15$) and the wavelength is that of the LSPR peak at that index. The effect of volume fraction of the NPs and film thickness on the intensity dynamic range is plotted in Fig. 3, which shows the results from tracking the LSPR peak calculated from Eq. (2); while Fig. 3(b) depicts the approximation when using Eq. (10).

The plots in Fig. 3(b) deviate from the exact peak tracking especially at the larger film thickness where the error in the phase term becomes more dominant. This error is mainly due to the fact that the wavelength is fixed in Eq. (10), while the LSPR peak location actually shifts over the operation range as in Fig. 4(a). That causes an error in the phase term in Eq. (10). This phase error becomes more significant as the thickness increases and hence the obvious deviation in the dynamic ranges from the actual tracking. The shift in the LSPR peak wavelength over the operation range brings forward another figure-of-merit, wavelength dynamic range.

$$\text{Wave. dynamic range} = \lambda_{\text{LSPR}, n_3 = 1.33} - \lambda_{\text{LSPR}, n_3 = 1} \quad (11)$$

In comparison to intensity, tracking the wavelength eliminates possible errors that could be caused by light power fluctuations. However, it requires using a spectrometer and tracking algorithm compared to direct intensity measurement with a photodetector. For the same structure used in Fig. 3, the calculated wavelength dynamic is depicted in Fig. 4.

Opposite to the intensity dynamic range, the wavelength dynamic range seems to reduce when increasing the particles volume fraction. The calculations show that the wavelength dynamic range is maximized with $d < 40$ nm. However, the intensity dynamic range is higher for $d > 90$ nm. The plots in Figs. 3 and 4 show that by embedding gold nanoparticles in a dielectric thin film results in the attainment of a real vapor sensor having the properties tunable with both film thickness and volume fraction of the nanoparticles in the film. When optimizing a sensor design, it is however desirable to have a several degrees of freedom with which the system response can be altered. One parameter, yet to be determined, is the LSPR responses of different metal nanoparticles.

Changing the Nanoparticle Material

In the previous section, two factors like volume fraction of the nanoparticles and film thickness were considered keeping the material type unaltered. Changing the material alters the LSPR properties and consequently is the material response to the environmental changes, as evident in the plots of intensity and wavelength dynamic range with copper nanoparticles ~~are used~~ instead of gold nanoparticles (Fig. 5). “Intensity dynamic range” in this case has a similar trend to that for gold nanoparticles. The “wavelength dynamic range” in Fig. 5(b), however, shows three distinct regions with zero crossings; two regions with relatively

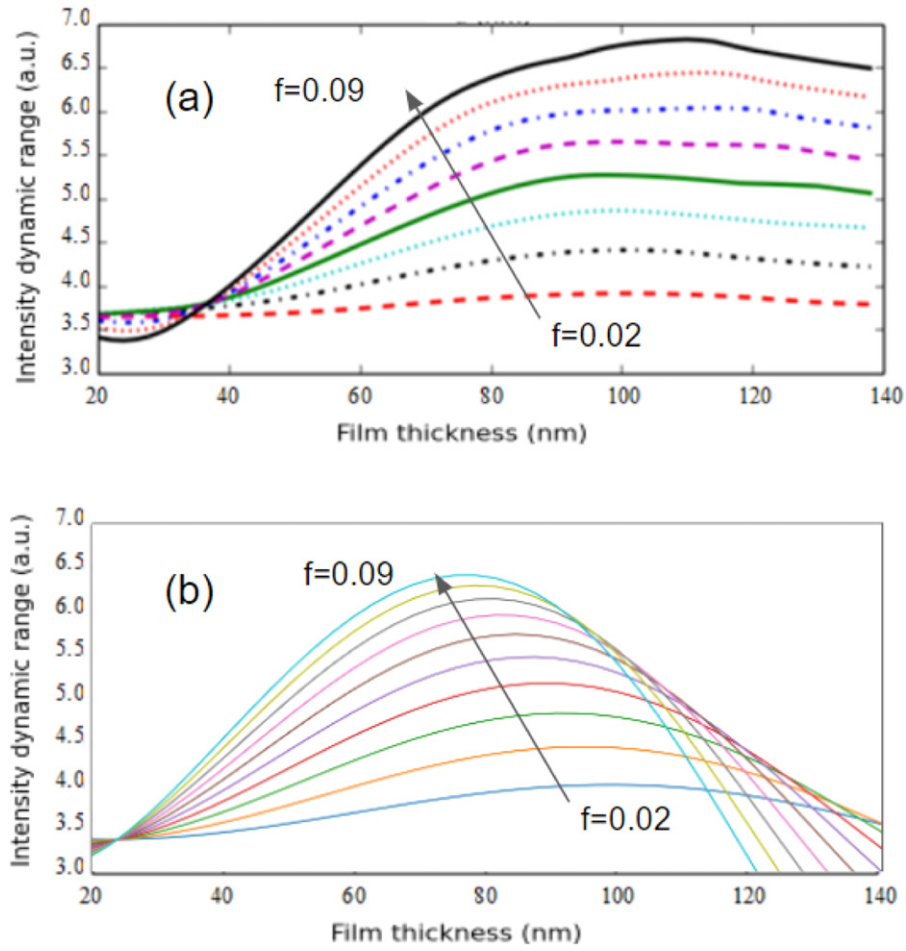


Fig. 3 Calculated intensity dynamic ranges when varying volume fraction from 0.02 to 0.09 and the film thickness from 20 nm to 140 nm for gold nanoparticles in a polymer over a glass substrate by (a) tracking the LSPR peak calculated using Eq. (2) and (b) using the approximation in Eq. (10).

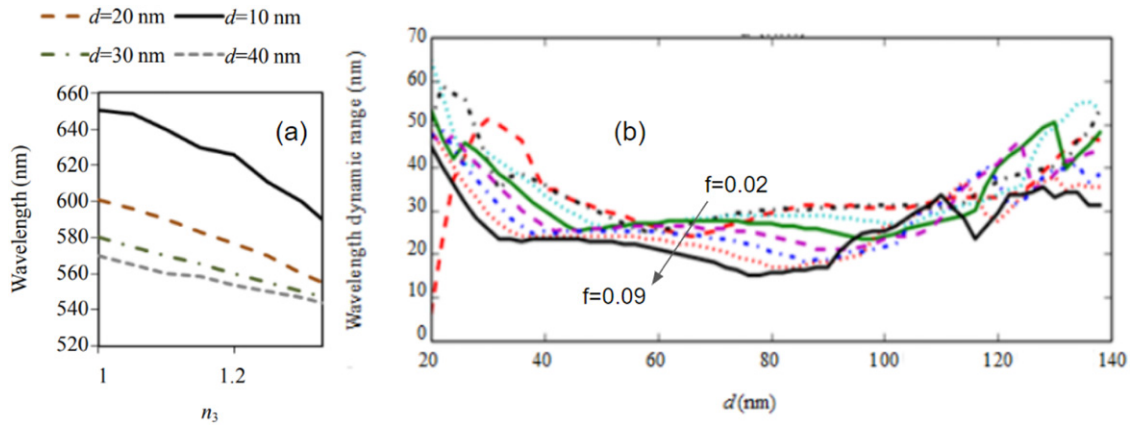


Fig. 4 (a) The shift of the LSPR wavelength with n_3 for different film thicknesses. (b) Calculated wavelength dynamic ranges when varying volume fraction from 0.02 to 0.09 and the film thickness from 20 nm to 140 nm for gold nanoparticles in a polymer over a glass substrate by tracking the LSPR peak calculated using Eq. (2).

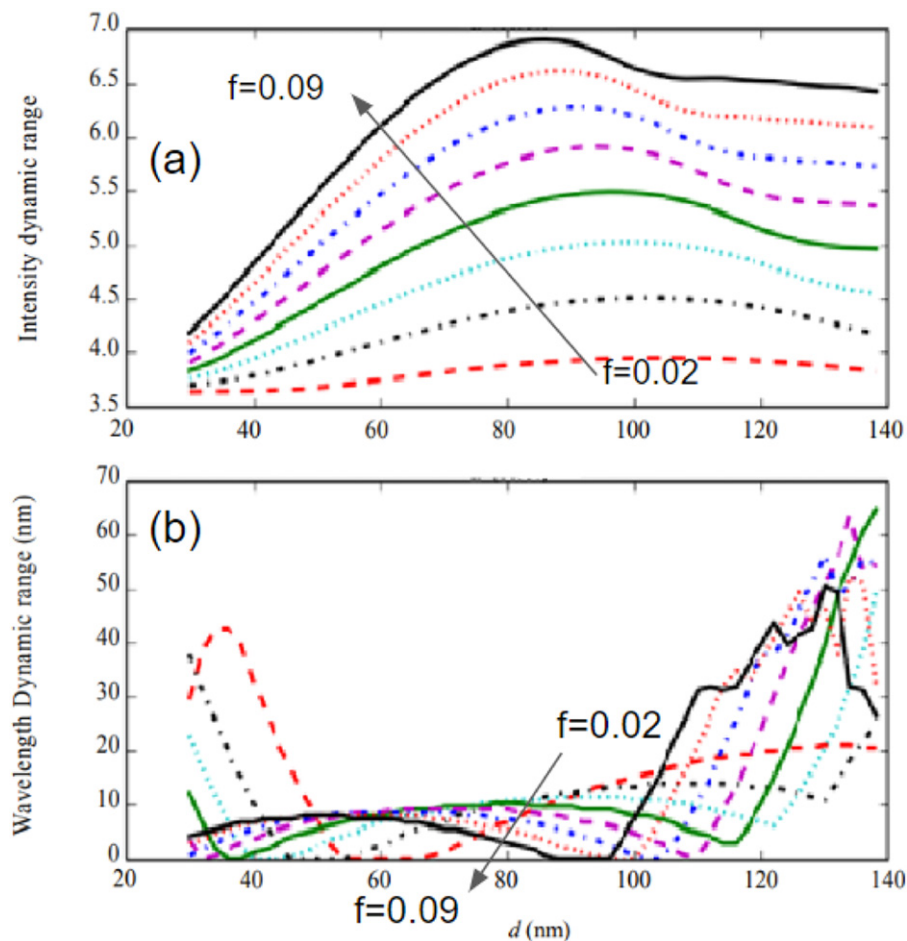


Fig. 5 (a) Intensity dynamic range and (b) wavelength dynamic range for copper nanoparticles when varying the volume fraction and film thickness.

high dynamic range at low and high film thicknesses and a middle region with relatively low dynamic range. As illustrated in Fig. 6, high wavelength dynamic is caused by the broadening of the plasmonic peak for both the low and high film thicknesses. This is not the case when the peak is defined, as in Fig. 6(b).

Large Nanoparticles

Previous section has discussed about nanoparticles that are very small compared to the wavelength and how to design an optical humidity sensor by embedding the nanoparticles in a dielectric film. The particles and the dielectric host generate a new effective medium with enhanced optical response to the change of the surrounding compared to the host alone. This enhancement comes from the presence of the LSPR at the interface of the metal particle and dielectric host. A thin film made from the effective medium forms a Fabry Perot interferometer. The effect of the environment on the LSPR peak in the reflection spectrum comes from the complex Fresnel reflection coefficient between the film and the superstrate.

In optimizing the optical sensor, the film thickness is varied from 20 nm to 140 nm. This is a feasible range of operation considering the nanoparticles to be very small. Considering 10% of the operation wavelength to be sufficiently small, the particle-size should be less than 35 nm (assuming 350 nm to be the start of the visible spectrum). Considering the limits of the thin film, much smaller particles are needed to form an effective homogeneous film. This is, however, not the case for the particles to be larger in size. It is not actually worth considering “effective medium analysis” for larger particles, as the scattering of light at this scale is unlikely. In order to design an optical sensor using larger particles, a study on the effect of environmental change on the scattering of light is needed.

Monolayer Film of Large Nanoparticles

The section deals with the theoretical investigations on the response of a simple transducer formed by a monolayer of large metal nanoparticles deposited on a glass substrate, in terms of vapor sensing applications. Similar to the thin film with small particles,

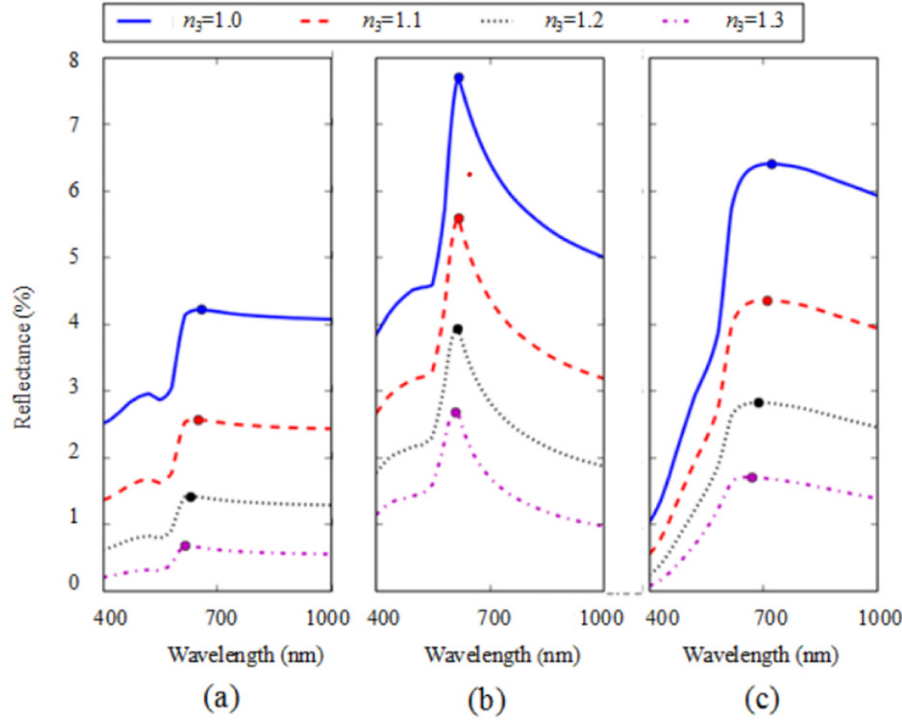


Fig. 6 Calculated reflection spectrum for Cu NPs in polymer with $f = 0.05$ at the film thicknesses of (a) 20 nm, (b) 80 nm, and (c) 140 nm.

this device utilizes the shift in the LSPR peak due to the presence of the vapor in the surrounding. Here, the metal NPs are considered to be spherical in shape with sizes larger than “Maxwell’s Garnett limit”. The layer thickness is assumed to be equal to the diameter of one nanoparticle (Fig. 7). In this case, however, one cannot assume a Fabry-Perot interferometer. Instead, the changes in the LSPR peak comes from the change of the scattering and attenuation properties of the individual particle. If the cross-talk between the particles is ignored, the total response is the collective responses from all particles. This approximation is valid in the structure proposed in Fig. 7, where the light scattering occurs on the surface and light excitation occurs from the bottom. The effect of cross-talk due to multiple scattering is minimal considering an interaction thickness equals to the diameter of a particle.

When measuring the transmitted light using a detector placed in the far-field, one can represent the effect of one particle by its extinction cross-section. The total attenuation coefficient, α , due to the collection of spherical NPs on the surface of the substrate can be defined as (Van De Hulst, 2003)

$$\alpha = \frac{3}{4\pi} \sum_j \frac{f_j C_{ext,j}}{a_j^3} \quad (11)$$

Where f_j , a_j and $C_{ext,j}$ are the volume fraction, particle radius and extinction cross-section of the j^{th} nanoparticle. Assuming the interaction region to be the average diameter of the particles $2a$, the transmittance, measured at the detector, can be expressed using Beer’s law as $T = (1 - R)e^{-2\alpha a}$

R is the Fresnel reflection between the substrate and the surrounding and defined as,

$R = \left| \frac{n_m - n_s}{n_m + n_s} \right|^2$ Here, n_m is the surrounding refractive index and n_s is the substrate refractive index.

Mei Scattering From Spherical Particles

The extinction coefficient of one particle can be derived using Mei scattering of spherical nanoparticles (Yusof et al., 2018).

$$C_{ext,j} = \frac{2\pi}{k^2} \sum_{n=1}^N (2n+1) \text{Re}\{a_{n,j} + b_{n,j}\} \quad (12)$$

where k is the propagation constant in the medium, $k = 2\pi/\lambda$. The coefficients $a_{n,j}$ and $b_{n,j}$ are defined as

$$a_{n,j} = \frac{m_j \psi_n(m_j x_j) \psi'_n(x_j) - \psi_n(x_j) \psi'_n(m_j x_j)}{m_j \psi_n(m_j x_j) \zeta'_n(x_j) - \zeta_n(x_j) \psi'_n(m_j x_j)} \quad (13a)$$

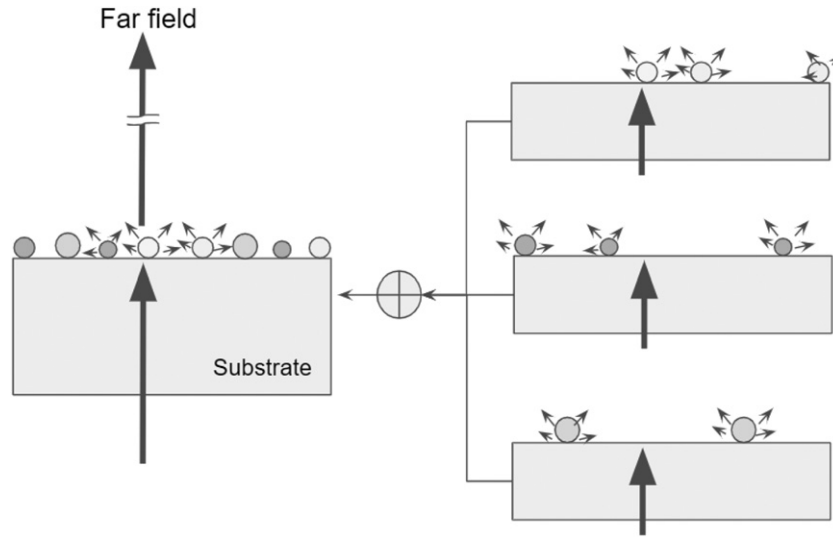


Fig. 7 Light scattering by a monolayer of large nanoparticles, where the monolayer thickness is equal to NP diameter.

$$b_{n,j} = \frac{\psi_n(m_j x_j) \psi'_n(x_j) - m_j \psi_n(x_j) \psi'_n(m_j x_j)}{\psi_n(m_j x_j) \zeta'_n(x_j) - m_j \zeta_n(x_j) \psi'_n(m_j x_j)} \quad (13b)$$

where $x_j = 2\pi n_m a_j / \lambda$, $m_j = n_{p,j} / n_m$ and $n_{p,j}$ is the j^{th} metal nanoparticle complex refractive index and n_m is the refractive index of the surrounding medium. $\psi_n(u) = u \cdot j_n(u)$ and $\zeta_n(u) = u \cdot h_n^{(1)}(u)$, where $j_n(u)$ is the “spherical Bessel function of the first kind” and $h_n^{(1)}(u)$ is the “spherical Hankle function of the first kind”. In Eq. (12), the upper limit N should be theoretically set to infinity. However, in the calculations, N is set to a finite value at which the computation converges. The proper value of N is expected to primarily depend on the particle size and the surrounding index to some extent.

Monolayer of identical particles

For the special case of a monolayer formed by identical particles, the transmittance can be written as

$$T = (1 - R) \exp\left(-\frac{3f}{2\pi a^2} C_{ext}\right) \quad (14)$$

In this case, the transmittance spectrum profile depends on C_{ext} , while the volume-fraction uniformly affects the amplitude of the total spectrum. This is mainly due to the fact that multiple scattering between particles is neglected. For the extinction coefficient in Eq. (12), in the case of identical particles j is omitted, one important factor is how many orders one should select for the calculations to converge. The transmittance of a monolayer of nanoparticles as a function of wavelength for different radii (20 nm, 60 nm and 100 nm) and varying order number (N) from 1 to 5 with $n_m = 1$ is shown in Fig. 8(a) and the calculated errors between 5th and 1st orders with n_m increasing from 1–1.33 are shown in Fig. 8(b).

For small particles, one order seems to be sufficient enough to calculate the extinction coefficient, as there is no observed deviation in the transmittance when increasing N . While increasing the particle size, a slight deviation is noticed for a radius of 60 nm. This deviation becomes pronounced for 100 nm particles. A second dip is clearly observed at a lower wavelength that does not present for $N = 1$. This dip is due to a higher order, $N = 2-5$. In order to quantify the deviation in transmittance, an error function is defined

$$Error = 100 \int_{\lambda_{min}}^{\lambda_{max}} \frac{T_5(\lambda) - T_1(\lambda)}{T_1(\lambda)} d\lambda \quad (15)$$

Where T_1 and T_5 are the calculated transmittance spectra when $N = 1$ and 5 respectively. The plots in Fig. 8(b) show that the error increases as the particle size increase as well as the surrounding refractive index, n_m , increases. For $n_m = 1$, the solution with one order is sufficient up to $a = 70$ nm (labeled by a_1 in the figure). As expected, the error is higher for 100 nm and 130 nm particles (labeled by a_2 and a_3 in the plots). Increasing n_m as well increases the error significantly. It is worth noting that for a solution-based detection where $n_m = 1.33$, the particles need to be smaller than 20 nm so that one order can be accurate enough to estimate the response of the monolayer to the incident light. Fig. 9 shows the effect of the first three orders on the transmittance for four different nanoparticle radii when varying n_m from 1 to 1.33.

The plots in Fig. 9(a) show almost no effect of the second order (hence the higher orders) on the total transmittance for 70 nm particles except when n_m approaches 1.33. Increasing the particle radius to 100 nm shows an obvious broadening of the first order dip, where a clear narrower second order is present. It is, however, less sensitive to the n_m changes compared to the first order. For

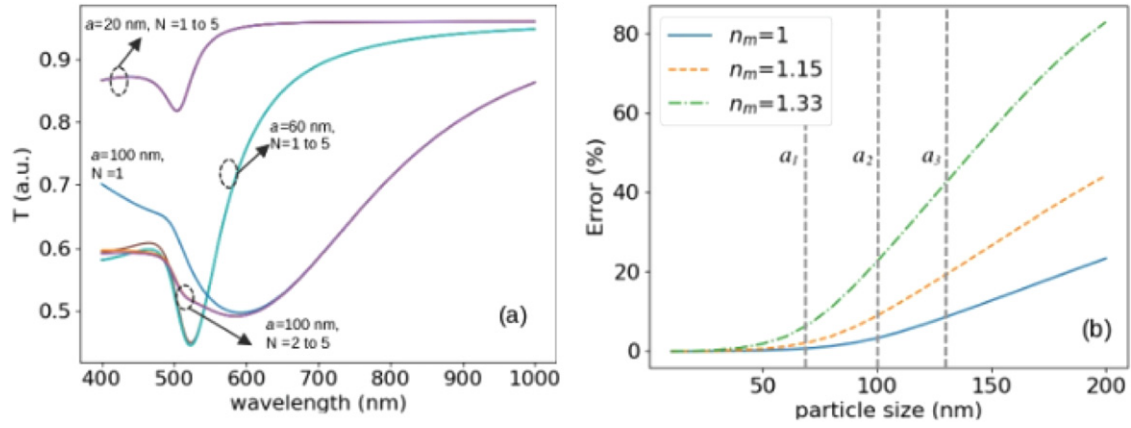


Fig. 8 (a) transmittance of a monolayer of nanoparticles with three different radii: 20 nm, 60 nm and 100 nm. The order number of varies from 1 to 5 with $n_m = 1$. (b) The calculated error between 5th and 1st orders when increasing n_m from 1–1.33.

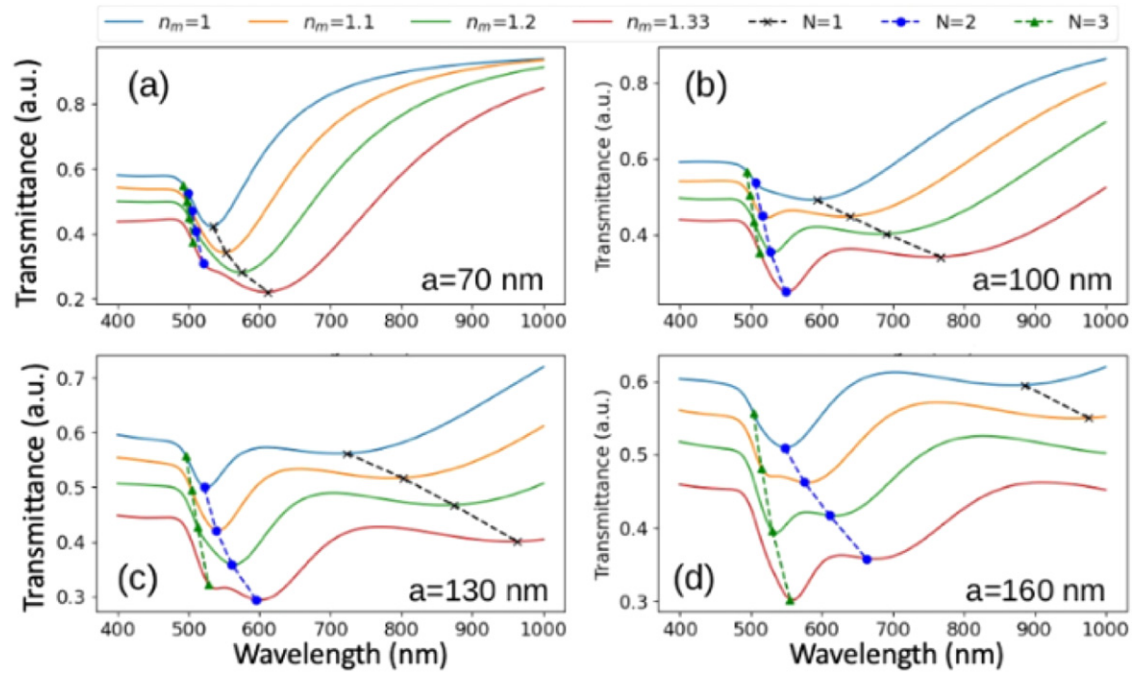


Fig. 9 The transmittance of a monolayer with volume fraction of 0.1 while varying the surrounding refractive index n_m for four different particle sizes: (a) 70 nm, (b) 100 nm, (c) 130 nm and (d) 160 nm.

larger particle size, the third order's effect is noticeable as in Figs. 9c-d. **Fig. 10** shows the transmittance for various radii of the particles (91 nm, 168 nm and 246 nm) with varying surrounding indices ($n_m = 1$ and $n_m = 1.33$).

The plots in **Fig. 9** also show that the wavelength dynamic range, defined as the difference between the dip-wavelength at $n_m = 1.33$ and $n_m = 1$, is always larger for the first order. It increases with the size of the particle. If the source of excitation is, however, limited to the visible spectrum (400 – 700 nm), a proper selection of the particle size and order would be needed to maximize of the wavelength dynamic range. As the LSPR dip wavelength increases with the particle size and n_m , the radius needed for maximum dynamic range is that which causes a dip at 700 nm when $n_m = 1.33$. For the first three orders that correspond to radii of 91 nm, 168 nm, 246 nm, respectively as shown in **Fig. 10**. The inset in the figure shows that the wavelength dynamic range is almost similar for the three radii. This is illustrated by the dotted arrows that indicates the shift of the LSPR dip when n_m increases from air to water. **Fig. 11** shows the amplitude dynamic range versus particle size and excitation wavelength for a monolayer of identical particles with $f = 0.1$. The contour plot in **Fig. 11(a)** shows a maximum dynamic range of 0.64 obtained for particle radius of 45 nm at an excitation wavelength of 562 nm, which is in the visible spectrum. There however exists a practical operation region within which the dynamic range is larger than 0.6. This region extends from particle radii of 33–54 nm. The operation wavelength range extends between 534 nm and 592 nm as shown in **Fig. 11(b)**.

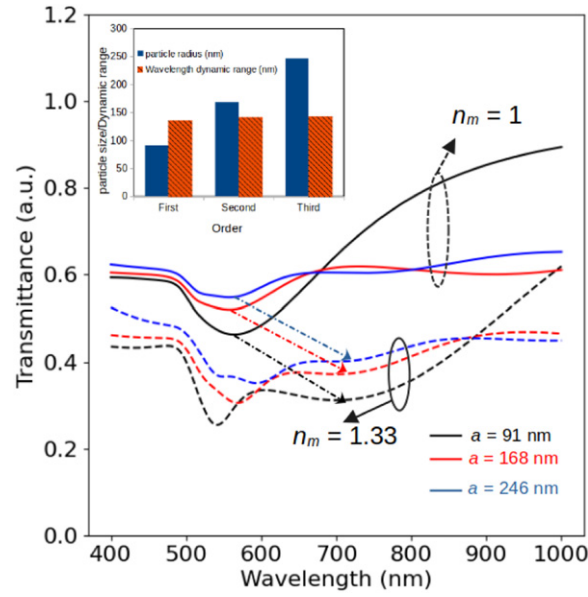


Fig. 10 The transmittance for three radii: 91 nm, 168 nm and 246 for two surrounding indices $n_m = 1$ and $n_m = 1.33$. The inset shows the radii and dynamic range when the transmittance has a dip at 700 nm due to the first three orders with f fixed at 0.1.

Effect of particle-size distribution

In practice, synthesizing nanoparticles typically results in size distribution around an average desired value that is measured from the scanning electron microscope (SEM) images. When considering a Gaussian distribution around an average radius of a_0 and a standard deviation of σ , Eq. (11) can be re-written as

$$\alpha = \frac{3}{\sigma a_0^3 (2\pi)^{3/2}} \int_r C_{ext}(r) \cdot \exp\left(-\frac{1}{2}\left(\frac{r-a_0}{\sigma}\right)^2\right) dr \quad (16)$$

The transmittance is then calculated using $T = (1 - R)e^{-2\alpha a}$ when replacing a by a_0 . Using Eq. (16), the effect of increasing the size distribution around an average radius of 45 nm is depicted in Fig. 12.

Fig. 12 shows the variation of transmittance and amplitude dynamic range with wavelength for varying standard deviation of particles' radii. As evidenced from Fig. 12(b), there is a decrease in the value of amplitude dynamic range and a broadening of the peak with a red shift, as the standard deviation of particles' radii increases.

Different Types of Identical Particles

One way to enhance the amplitude dynamic range, and hence the sensitivity, of the monolayer device is through combining nanoparticles of different materials. Here, a combination of gold, silver and copper nanoparticles are used. The particle sizes are set to 45 nm. The target here is to realize a practical dynamic range over a large bandwidth of the visible spectrum. This allows the use of sun light for passive devices as well as off-shelf light sources, such as LED's and laser diodes, for active optical sensor. In order to increase the degrees of freedom for achieving such a design, three different nanoparticles of Au, Ag and Cu with same radius are selected. The transmittance of a monolayer film can then be expressed as in Eq. (17).

$$T = (1 - R) \exp\left(-\frac{3}{2\pi a^2} \sum_{j=1}^M f_j \cdot C_{ext,j}\right) \quad (17)$$

where M is the number of particle types. In this case, $M = 3$. Using Eq. (17), the Fig. 13 shows the effect of varying volume fraction gold particles from 0 to 0.1 while fixing that of silver and copper at 0.1. The figure shows an almost flat dynamic range around 0.55 over most of the visible spectrum when only Cu and Ag particles are used. The bandwidth reduces when the volume fraction of gold nanoparticles increases. Fig. 13(c) shows the estimated color of the transmitted light (considering an incident white light and transferring the spectrum into RGB values) for the different gold volume fractions when changing the surrounding from air to water. The graphs show a visible color contrast. Hence, this configuration can allow the use of the composed thin film of nanoparticles as a passive indicator for humidity or vapor in a specific environment. If the film, with 0.1 vol fraction of nanoparticles with a composition of Cu, Ag and Au having average radius of 45 nm, is coated on a white glossy sheet, the color of the film will change from beige to dark maroon if the surface is wet. Shades in between will indicate the level of humidity of the

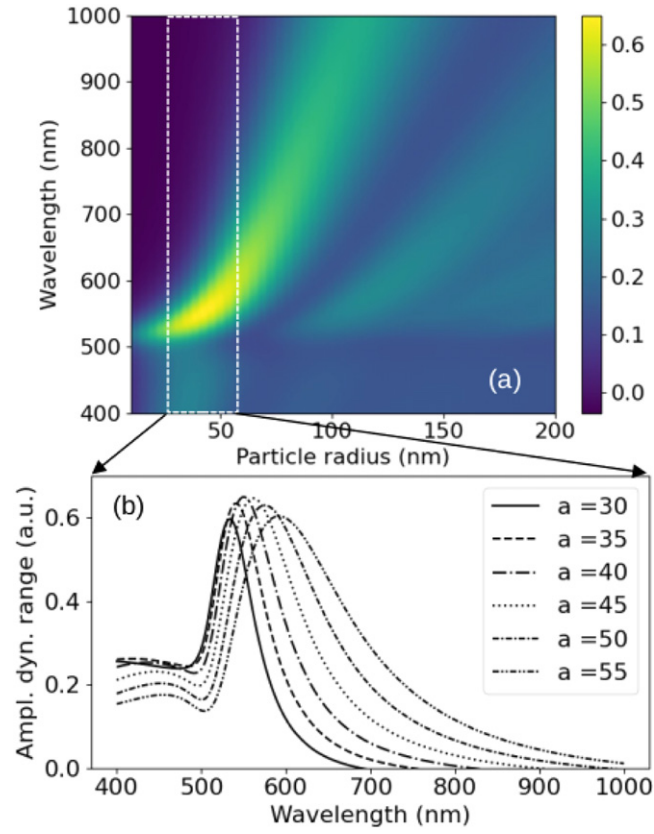


Fig. 11 (a) Amplitude dynamic range versus particle size and excitation wavelength or a monolayer of identical particles with $f = 0.1$. (b) Zoom on the practical region between 30 nm and 50 nm particle radii.

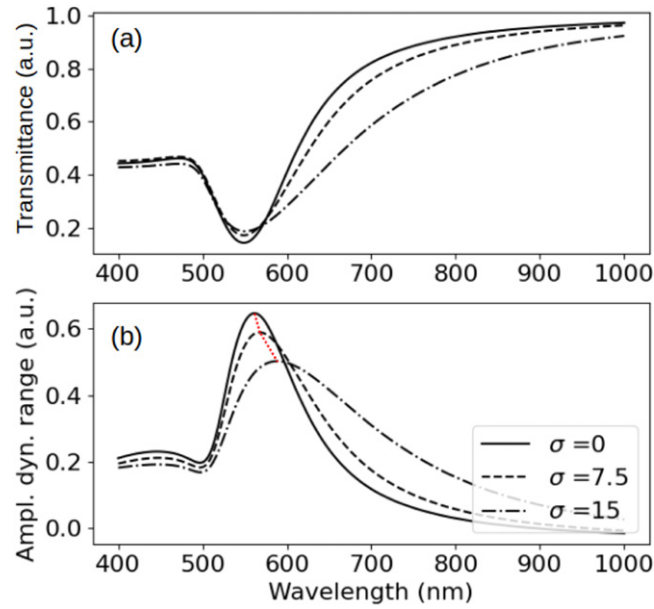


Fig. 12 Effect of increasing the standard deviation of particles radii that follows a Gaussian distribution on (a) transmittance at $n_m = 1.33$ and (b) amplitude dynamic range. The average particle radius is 45 nm and the volume fraction is set to $f = 0.1$.

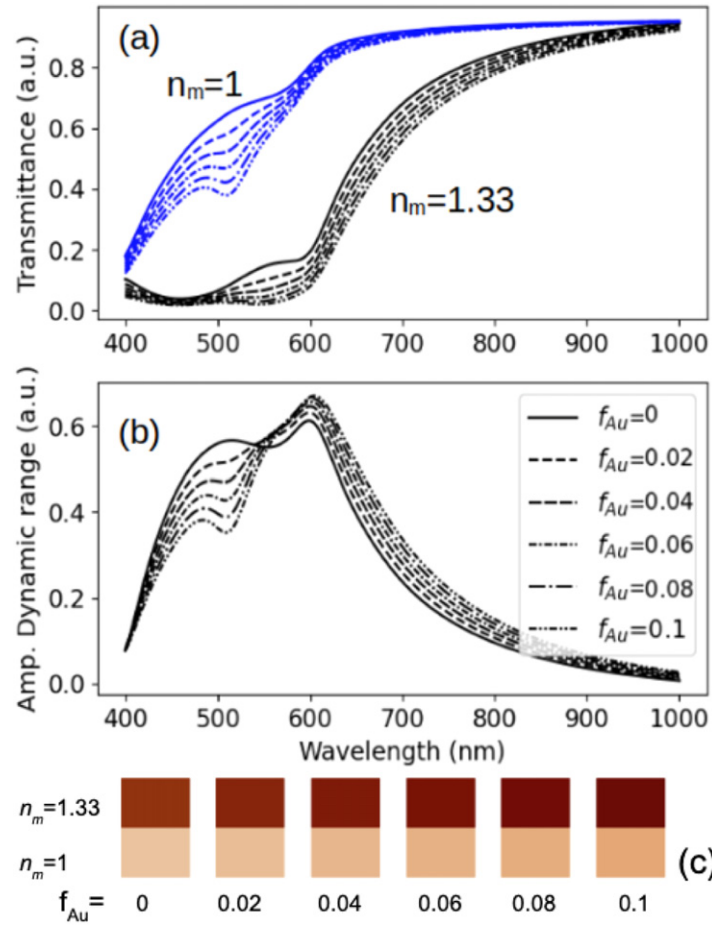


Fig. 13 The effect of varying gold volume fraction from 0 to 0.1 while fixing those of silver and copper on (a) transmittance at $n_m = 1$ and 1.33 and (b) amplitude dynamic range. The average particles radius is 45 nm. (c) The estimated color of the film when exposed to air and water for the different gold volume fractions.

surrounding environment. This could be placed, for example, near the water of the liquid pipes to get a visual indication of potential leakage, if any.

Fig. 14 shows the effect of volume fractions (from 0 to 0.1) of Ag and Cu nanoparticles on the dynamic range for invariant volume fractions of the particles. Narrow bandwidth of the dynamic range is sustained with the variation of the volume fractions of silver and copper nanoparticles, as evidenced in **Fig. 14**. The wavelength with maximum dynamic range, however, seems to be affected mainly by copper, as indicated in **Fig. 14**(b). The color contrast in **Fig. 14**(c) shows a response similar to **Fig. 13**(c) with a slight improvement in the color contrast between air and water.

Particles Deposited on a Homogeneous Thin Film

Using the Fabry Perot equation, the effect of the particles on top of the film can be introduced through the reflection coefficient

$$r_{23} = r_{Mei}(\pi) \cdot \left(\frac{n_2 - n_3}{n_2 + n_3} \right) \quad (18)$$

where, r_{Mei} is Mei correction for large particle.

$$r_{Mei}(\pi) = \frac{E_{s\theta}(\theta = \pi, \phi = 0)}{E_o} = \frac{1}{kr} \sum_{n=1}^{\infty} \frac{E_n}{E_o} (ia_n \zeta'_n(x) \tau_n - b_n \zeta_n(x) \pi_n)_{\theta = \pi, \phi = 0} \quad (19)$$

$$\tau_n = -n\pi_n - (n+1)\pi_{n-1}. \quad (20)$$

$$\pi_n = -\frac{2n-1}{n-1}\pi_{n-1} - \frac{n}{n-1}\pi_{n-2}$$

knowing that $\pi_0 = 0$ and $\pi_1 = 1$.

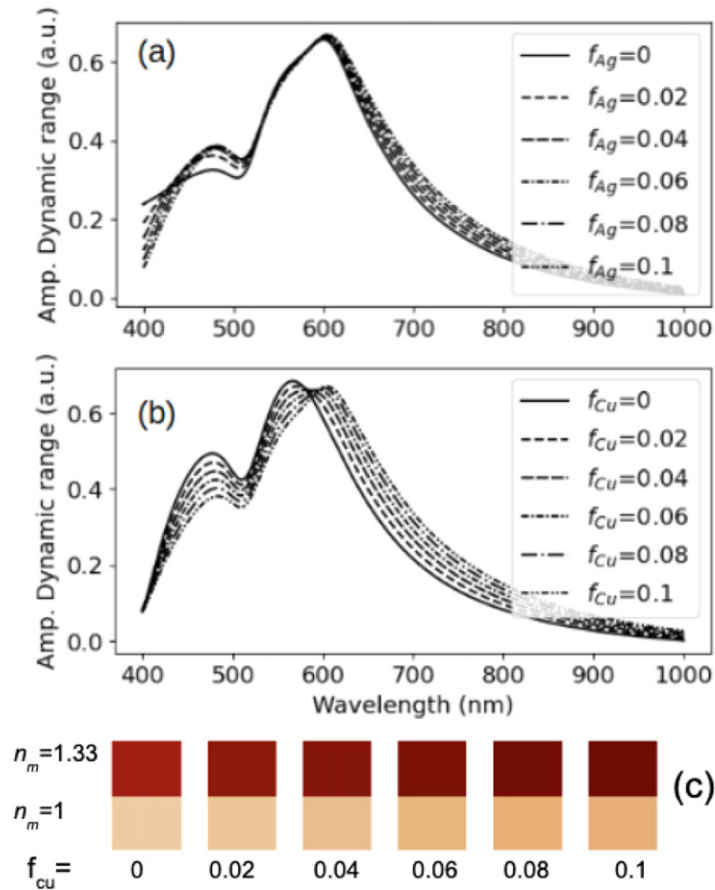


Fig. 14 The effect of varying (a) Silver and (b) Copper volume fractions from 0 to 0.1 while fixing the other two metals volume fraction on the dynamic range. The average particles radius is set to 45 nm for all particles (c) The estimated color of the film when exposed to air and water for the different copper volume fractions.

Transmittance in the far-field is

$$T = (1 - R_{FP}) \cdot \exp(-\alpha \cdot a) \quad (21)$$

Where R_{FP} is the reflectance power.

Conclusion

A characteristic photonic sensor based on metal nanoparticle-embedded thin films has been projected in this article. The sensitivity is measured using the changes of reflectance with respect to the refractive index of the material. Various effects on the performance of the sensor have been studied considering the variation in size and volume fraction of the nanoparticles, filling factor, material type, etc. Nanoparticles are embedded in a polymer film deposited over a substrate where the superstate is considered the sensing material. Sensitivity is calculated using appropriate equations for nanoparticles smaller than the wavelength, where the shape of the nanoparticles is considered to be spherical. Noticeable effect has been observed on the sensing ability on changing the material type of the nanoparticles, film thickness and filling factor, irrespective of one another. When the size of the nanoparticle increases and is equal to the film thickness, the Mei parameter is considered so as to get the effect of the particle in the transmission, as calculated in the case of smaller particles using Fabry Perot equation. However, in order to get a more systematized effect on the sensitivity, different shapes and sizes of the nanoparticles of various types are yet to be considered in a systematic manner.

References

- Benelmekki, M., 2015. Designing Hybrid Nanoparticles. Morgan & Claypool Publishers.
- Buvailo, A.I., Xing, Y., Hines, J., Dollahon, N., Borguet, E., 2011. TiO₂/LiCl-based nanostructured thin film for humidity sensor applications. ACS Applied Materials & Interfaces 3 (2), 528–533.

- Chen, W., Zhang, J.Z., Joly, A.G., 2004. Optical properties and potential applications of doped semiconductor nanoparticles. *Journal of Nanoscience and Nanotechnology* 4 (8), 919–947.
- Cheng, B., Tian, B., Xie, C., Xiao, Y., Lei, S., 2011. Highly sensitive humidity sensor based on amorphous Al₂O₃ nanotubes. *Journal of Materials Chemistry* 21 (6), 1907–1912.
- Drabik, M., Vogel-Schäuble, N., Heuberger, M., Hegemann, D., Biederman, H., 2013. Sensors on textile fibres based on Ag/a-C:H:O nanocomposite coatings. *Nanomaterials and Nanotechnology* 3, 1–8.
- Gurban, A.M., Burtan, D., Rotariu, L., Bala, C., 2015. Manganese oxide based screen-printed sensor for xenoestrogens detection. *Sensors & Actuators B: Chemical* 210, 273–280.
- Kuang, Q., Lao, C., Wang, Z.L., Xie, Z., Zheng, L., 2007. High-sensitivity humidity sensor based on a single SnO₂ nanowire. *Journal of the American Chemical Society* 129 (19), 6070–6071.
- Kumar, G.S.R., J. V.R., 2013. Thin film deposition, formation of nanoparticles & variation of resistance of deposited sample with temperature. *International Journal of Nanotechnology and Application* 3, 1–10.
- Lee, H., Wang, C., Lin, C., 2014. High-performance humidity sensors utilizing dopamine biomolecule-coated gold nanoparticles. *Sensors and Actuators B* 191, 204–210.
- Liu, Z., Zhong, Y., Shafei, I., *et al.*, 2019. Tuning infrared plasmon resonances in doped metal-oxide nanocrystals through cation-exchange reactions. *Nature Communications* 1394, volume 10, Article number.
- McFarland, A.D., Van Duyne, R.P., 2003. Single silver nanoparticles as real-time optical sensors with zeptomole sensitivity. *Nano Letters* 3 (8), 1057–1062.
- Miao, F., Tao, B., Sun, L., *et al.*, 2010. Capacitive humidity sensing behavior of ordered Ni/Si microchannel plate nanocomposites. *Sensors and Actuators A: Physical* 160 (1–2), 48–53.
- Mogera, U., Sagade, A.A., George, S.J., Kulkarni, G.U., 2014. Ultrafast response humidity sensor using supramolecular nanofibre and its application in monitoring breath humidity and flow. *Scientific Reports* 4, 1–9.
- Ngo, H.V., Tran, Ph.H.L., Lee, B., Tran, T.T.D., 2019. Development of film-forming gel containing nanoparticles for transdermal drug delivery. *Nanotechnology* 30 (41), 415102.
- Nielsen, S., 2003. *Food Analysis*. vol. 5. New York: Springer Science & Business Media.
- Power, A.C., Betts, A.J., Cassidy, J.F., 2010. Silver nanoparticle polymer composite based humidity sensor. *Analyst* 135 (7), 1645–1652.
- Rao, M.C., Shekhawat, M.S., 2013. A brief survey on basic properties of thin films for device application. *International Journal of Modern Physics* 22, 576–582. (Conference Series).
- Sahi, S., Magill, S., Ma, L., *et al.*, 2018. Wavelength-shifting properties of luminescence nanoparticles for high energy particle detection and specific physics process observation. *Scientific Reports* 8 (1), 10515.
- Thiawong, T., Onlaor, K., Tunhoo, B., 2013. A humidity sensor based on silver nanoparticles thin film prepared by electrostatic spray deposition process. *Advances in Materials Science and Engineering*. 1–7.
- Van De Hulst, H.C., 2003. *Light Scattering by Small Particles*. Dover Publications Inc.
- Yakubu, I.S., Muhammad, U., Muhammad, A.A., 2018. Humidity sensing study of polyaniline/copper oxide nanocomposites. *International Journal of Advanced Academic Research Sciences: Technology & Engineering* 4 (5), 49–61.
- Yusof, H.H.M., Harun, S.W., Dimyati, K., *et al.*, 2018. Optical dynamic range maximization for humidity sensing by controlling growth of zinc oxide nanorods. *Photonics and Nanostructures – Fundamentals and Applications* 30, 57–64.